Supplementary Information

Opto-thermoelectric nanotweezers

Linhan Lin[1,2,†], Mingsong Wang[1,†], Xiaolei Peng[2,†], Emanuel N. Lissek[3], Zhangming Mao[4], Leonardo Scarabelli[5,6], Emily Adkins[7], Sahin Coskun[8], Husnu Emrah Unalan[8], Brian A. Korgel[7], Luis M. Liz-Marzán[5,9,10], Ernst-Ludwig Florin[3] and Yuebing Zheng[1,2,*]

[1]Department of Mechanical Engineering, The University of Texas at Austin, Austin, TX 78712, USA.

[2]Materials Science & Engineering Program and Texas Materials Institute, The University of Texas at Austin, Austin, TX 78712, USA.

[3]Center for Nonlinear Dynamics, Department of Physics, The University of Texas at Austin, Austin, TX 78712, USA.

[4]Department of Engineering Science and Mechanics, The Pennsylvania State University, University Park, PA 16802, USA.

[5]Bionanoplasmonics Laboratory, CIC biomaGUNE, Paseo de Miramón 182, 20014 Donostia-San Sebastián, Spain.

[6]California NanoSystems Institute, University of California, Los Angeles, Los Angeles, California 90095, United States

[7]Department of Chemical Engineering, The University of Texas at Austin, Austin, TX 78712, USA.

[8]Department of Metallurgical and Materials Engineering, Middle East Technical University, Ankara 06800, Turkey.

[9]Ikerbasque, Basque Foundation for Science, 48013 Bilbao, Spain

[10]CIBER de Bioingeniería, Biomateriales y Nanomedicina, CIBER-BBN, 20014 Donostia-San Sebastián, Spain

[†]These authors contributed equally to this work.

[*]E-mail: zheng@austin.utexas.edu

Supplementary Movies

Supplementary Movie 1: Real-time trapping, dynamic transport and releasing of a single 100 nm Ag nanosphere (AgNS).

Supplementary Movie 2: Parallel trapping of six 100 nm AgNSs into a circle.

Supplementary Movie 3: Trapping and rotation of a single Ag nanowire (AgNW).

Supplementary Figures

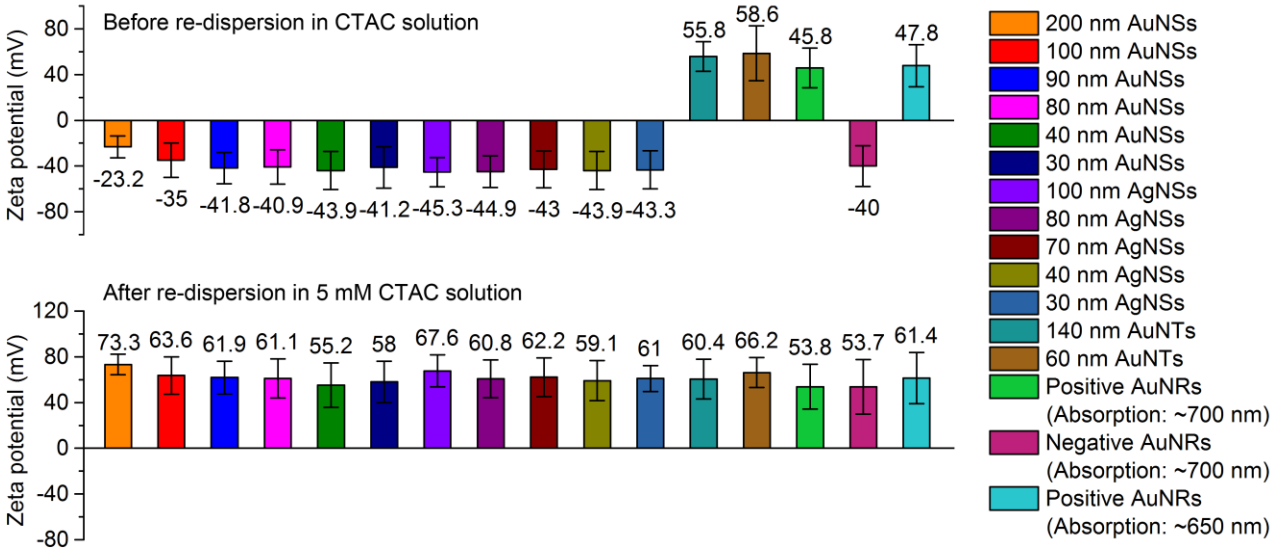

Supplementary Figure 1. Measured zeta potentials of different metal nanoparticles before and after re-dispersion in CTAC surfactant. Before re-dispersion, AuNSs with diameters from 40 nm to 200 nm were stabilized in 0.1 mM PBS solution. 30 nm AuNSs and AgNSs were stabilized in citrate solution, AuNTs were stabilized in 10 mM CTAC solution, and positive and negative AuNRs were dispersed in water. After centrifugation, the particles were re-dispersed in 5 mM CTAC solution.

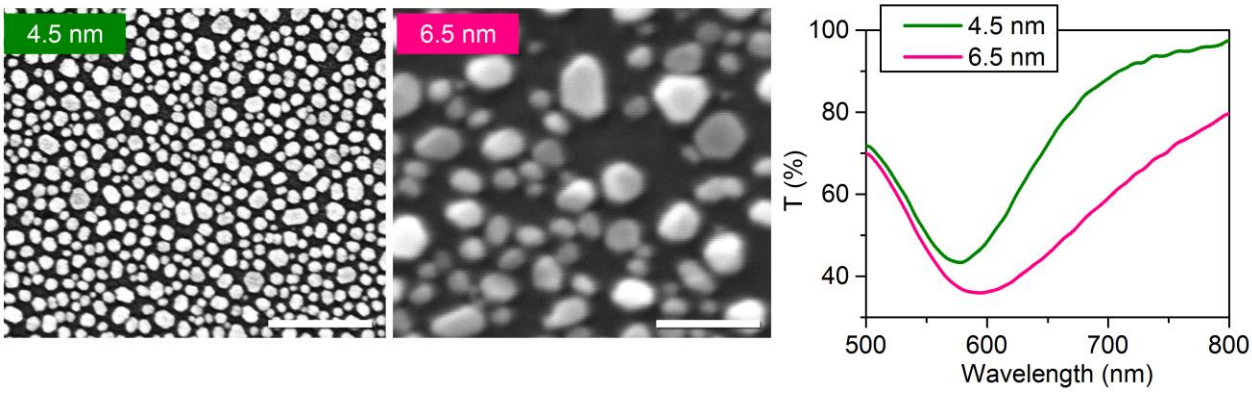

Supplementary Figure 2. Scanning electron micrographs (SEM) of porous Au films after thermal annealing of 4.5 nm and 6.5 nm (in thickness) Au thin films (left and middle panels) and the corresponding transmission spectra (right panel). The porous Au film was chosen since it features high photothermal conversion efficiency due to the excitation of a high-density of "hot spots" (plasmonically coupled Au nanoparticles) and low thermal conductivity because of the spatially isolated nanoparticle clusters on the substrate. Therefore, the porous Au film can lead to a high temperature gradient with a low-power light irradiation and temperature increment. Scale bars: 200 nm.

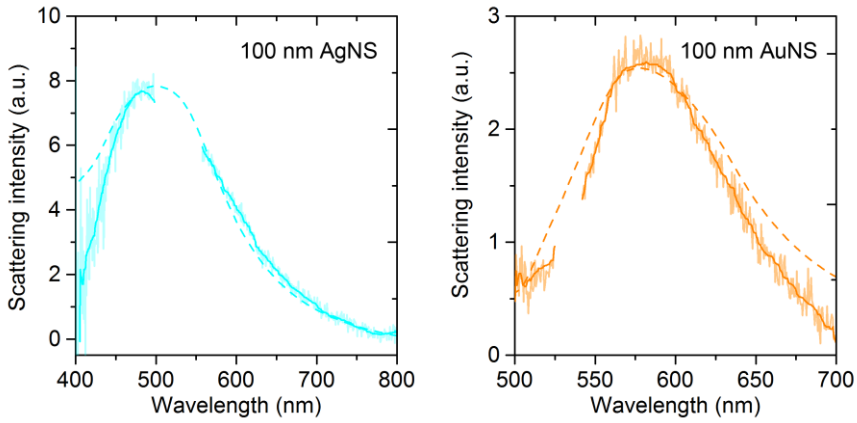

Supplementary Figure 3. *In-situ* scattering spectra of a 100 nm AgNS and a 100 nm AuNS trapped with a 532 nm laser beam. The solid (with and without smoothing) and dashed curves are the experimental and simulated spectra, respectively. A 533 nm notch filter was used to block the laser beam during the measurement.

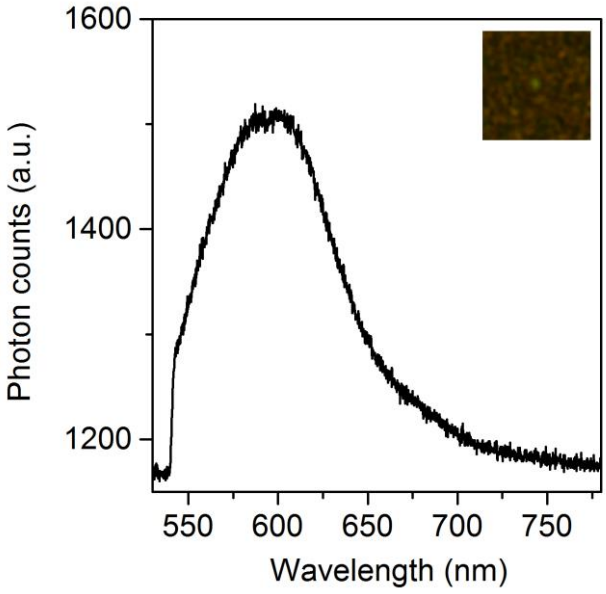

Supplementary Figure 4. Background spectrum of the thermoplasmonic substrate recorded under irradiation by the 532 nm laser beam without trapping of any particle.

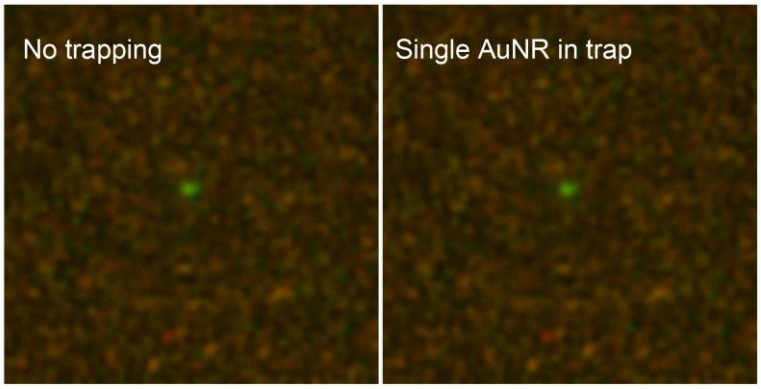

Supplementary Figure 5. Dark-field optical images recorded before and after a single Au nanorod (AuNR) was trapped by a single 532 nm laser beam. The scattering intensity of the AuNR is much weaker than the reflected laser beam and the fluorescence light from the thermoplasmonic substrate, preventing the observation of the red colour from the single AuNR.

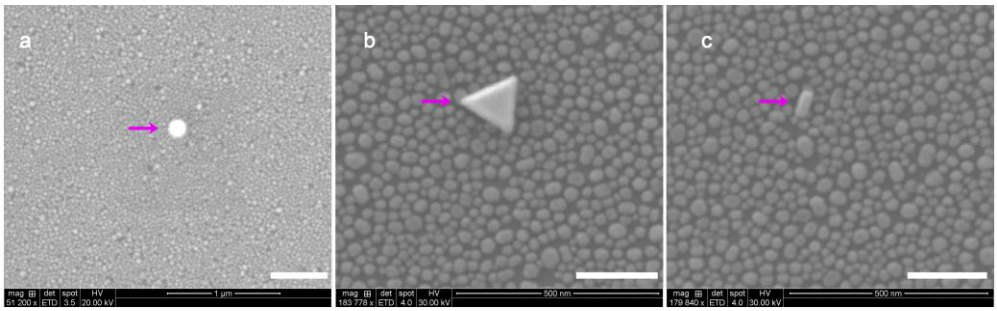

Supplementary Figure 6. SEM of single metal nanoparticles printed on the thermoplasmonic substrates after being trapped by the opto-thermoelectric nanotweezers (OTENT). a, single 100 nm AuNS; **b**, single 150 nm Au nanotriangle (AuNT); **c**, single AuNR. We printed the particles on the substrates by increasing the optical power after the particles were trapped at the laser spot, which significantly increases the trapping force to lock the particles on the substrate. After being rinsed and dried, the samples were imaged using SEM. These micrographs further verified the single nanoparticles trapped by our OTENT. The printed particles are indicated by the arrows. Scale bars: **a**, 500 nm; **b**-**c**, 200 nm.

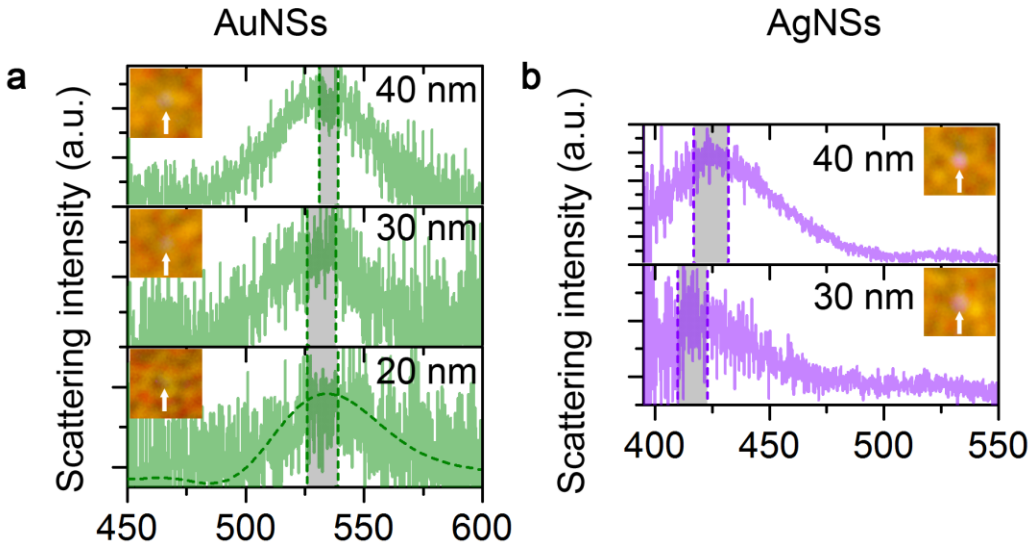

Supplementary Figure 7. Size-limit analysis of OTENT. Dark-field optical images and experimental scattering spectra of single **a,** AuNSs and **b,** AgNSs with diameters ranging from 20 to 40 nm.

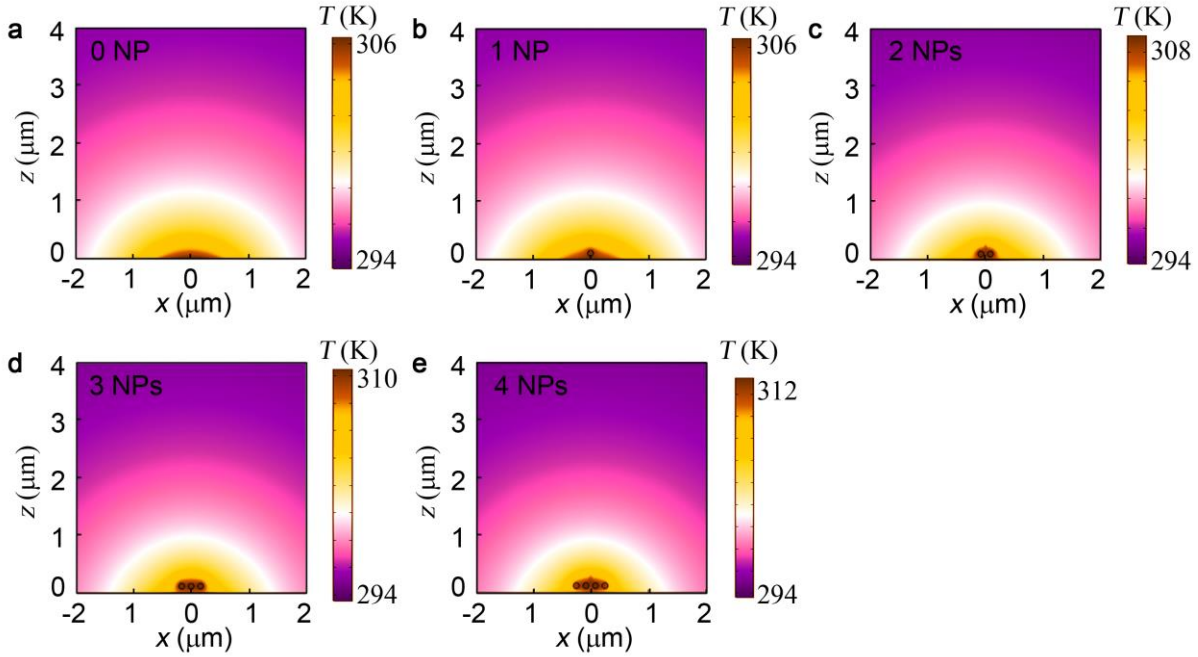

Supplementary Figure 8. Simulated temperature distributions before and after trapping of 100 nm AuNSs. The temperature cross sections in the *xz* plane were simulated with different number of 100 nm AuNSs trapped: **a,** 0 nanoparticle (NP); **b,** 1 NP; **c,** 2 NPs; **d,** 3 NPs; **e,** 4 NPs. The incident laser beam has a diameter of 2 μm and an optical power of 0.216 mW.

Supplementary Notes

Supplementary Note 1. Optical generation of thermoelectric field in OTENT.

The migration of ions under the temperature gradient is associated with the heat transfer between the ions and the surrounding environment, i.e. the heat will be absorbed from the reservoir at *T*, and given out at the temperature $T+\Delta T$, which provides the possibility to maintain a temperature gradient during the ionic transport[1]. The quantity of heat absorbed from the surroundings when one mole of ions is transferred is defined as the ionic heat of transport Q^* , which creates a current along the temperature gradient[2]:

$$J(\mathrm{Cl^-}) = -D_{\mathrm{Cl^-}}(\nabla n_{\mathrm{Cl^-}} + n_{\mathrm{Cl^-}}\frac{Q^*_{\mathrm{Cl^-}}}{k_{\mathrm{B}}T^2}\nabla T - n_{\mathrm{Cl^-}}\frac{Z_{\mathrm{Cl^-}}eE_0}{k_{\mathrm{B}}T}) \quad (1)$$

where $D_{\mathrm{Cl^-}}$ is the diffusion coefficient of $\mathrm{Cl^-}$ ions, $n_{\mathrm{Cl^-}}$ is the concentration of $\mathrm{Cl^-}$ ions, T is the environmental temperature, $Z_{\mathrm{Cl^-}}$ is the charge number of the $\mathrm{Cl^-}$ ions, e is the elemental charge, E_0 is the electric field, $\nabla n_{\mathrm{Cl^-}}$ is the concentration gradient of $\mathrm{Cl^-}$ ions, $Q^*_{\mathrm{Cl^-}}$ is the heat of transport of $\mathrm{Cl^-}$ ions, k_{B} is the Boltzmann constant and ∇T is the temperature gradient. The Soret coefficient of the $\mathrm{Cl^-}$ ions $S_{\mathrm{T}}(\mathrm{Cl^-})$ is given as $7.18\times10^{-4}\ \mathrm{K^{-1}}$. The CTAC micelles are driven along the temperature gradient by thermophoresis[3], with a micelle Soret coefficient[4]:

$$S_{\mathrm{T}}(\mathrm{micelle}) = \frac{\varepsilon\zeta^2_{\mathrm{mic}}}{8\eta T D_{\mathrm{mic}}} \quad (2)$$

where ε and η are the dielectric constant and the viscosity of the solvent, respectively. D_{mic} and ζ_{mic} are the diffusion coefficient and the surface potential of CTAC micelles, respectively. At the steady state, the spatial redistribution of both CTAC micelles and $\mathrm{Cl^-}$ ions generates an electric field, which is given by[5]

$$E_{\mathrm{T}} = \frac{k_{\mathrm{B}} T \nabla T}{e} \frac{\sum_i Z_i n_i S_{\mathrm{T}i}}{\sum_i Z_i^2 n_i} \tag{3}$$

i indicates the ionic species, i.e. CTAC micellar ions or Cl^- ions. Since the CTAC micelle has a higher molecular mass and a larger Soret coefficient than the Cl^- ions, i.e. S_T (micelle) ~10^{-2} K^{-1} > S_T (Cl^-) ~7.18×10^{-4} K^{-1}, we obtain an electric field E_T pointing towards the laser beam from the spatial redistribution of both the CTAC micelles and the Cl^- ions[6], which can trap the positively charged metal nanoparticle at the laser spot.

Supplementary Note 2. Excluding depletion attraction and optical force as the main driving force in OTENT.

Depletion attraction interactions help trapping the nanoparticle. However, this is not the driving force in OTENT. For further verification, we replaced CTAC with a non-ionic surfactant, Triton X-100. We did not observe particle trapping for various Triton X-100 concentrations above its cmc, indicating that the electric field arising from the ionic surfactant is the driving force behind the observed particle trapping in OTENT. It should also be noted that OTENT is operated at low optical power with a correspondingly small optical gradient force (Supplementary Fig. 9), which can be ignored at optimized CTAC concentration (*i.e.*, 20 mM). However, at the CTAC concentration of 1-2 mM, the optical gradient force can play an important role because the thermoelectric trapping force is also small.

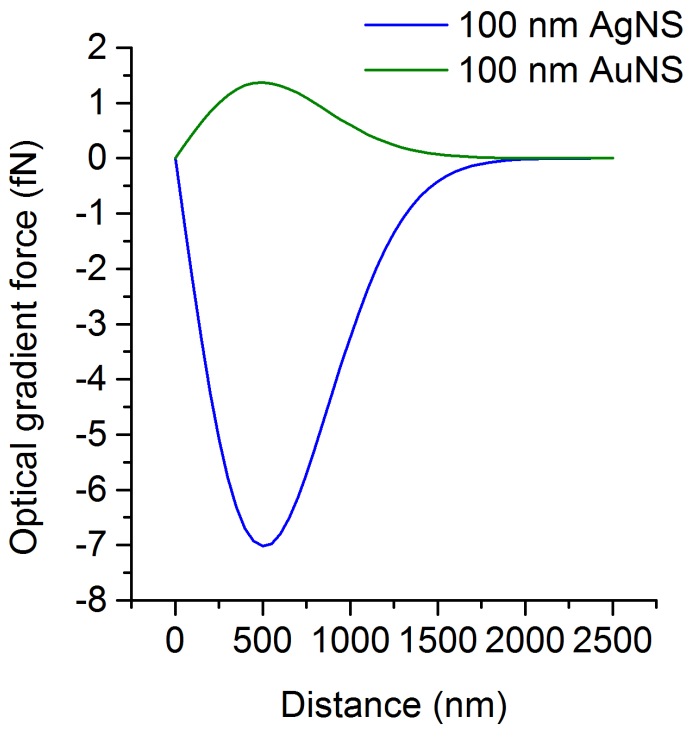

Supplementary Figure 9. Simulated optical gradient force exerted on a single 100 nm AgNS and a single 100 nm AuNS as a function of the in-plane distance to the beam centre. The incident laser beam has a diameter of 2 μm, a wavelength of 532 nm, and an optical power of 0.216 mW.

Supplementary Note 3. Calculation of the particle-substrate and particle-particle total interaction potential for 100 nm AuNSs.

In Supplementary Note 3, we give the derivation of the total interaction potential between two 100 nm AuNSs in the trap. In order to calculate the particle-substrate interaction potential which is critically important to estimate the trapping potential at high CTAC concentration, we treat the porous Au film as a wall, and the particle-substrate (or particle-wall) interaction potential can be easily obtained since it is about two times larger than the particle-particle interaction[7].

1. Electrostatic interaction.

The electrostatic interaction between two 100 nm AuNSs are given by[8]

$$U_{\mathrm{e}} = 32\pi\varepsilon r_{\mathrm{p}}\left(\frac{k_{\mathrm{B}}T}{ze}\right)^2\left[\tanh\left(\frac{ze\psi_{\mathrm{p}}}{4k_{\mathrm{B}}T}\right)\right]^2\exp(-\kappa r) \tag{4}$$

where ε is the solvent permittivity, r_{p} is particle radius, k_{B} is the Boltzmann constant, T is the absolute temperature, z is the particle charge valence, e is the elemental charge, ψ_{p} is the surface potential of the particle, which is a function of the CTAC concentration, κ is the inverse Debye length determined by the ionic strength, and r is the particle surface-to-surface distance. Above the critical micelle concentration (c_{cmc}, ~0.13 for CTAC)[9], κ is a function of c_{cmc} and the CTAC concentration, which is given by[10]

$$\kappa = [N_{\mathrm{A}}e^2 / \varepsilon k_{\mathrm{B}}T(\sum z_i c_{\mathrm{cmc}} + (c_{\mathrm{s}} - c_{\mathrm{cmc}})\omega)]^{1/2} \tag{5}$$

where N_{A} is the Avogadro's number, z_i is the valence of the surfactant cations and counterions, c_{s} is the CTAC concentration, and ω is the fraction of dissociated counterions, which is estimated as 0.25. Taking into full consideration the CTAC concentration dependent surface potentials (40-100 mV when the CTAC concentration increases from 0.2 mM to 20 mM), we calculated the electrostatic interaction potentials at different CTAC concentrations, as shown in Supplementary Fig. 10.

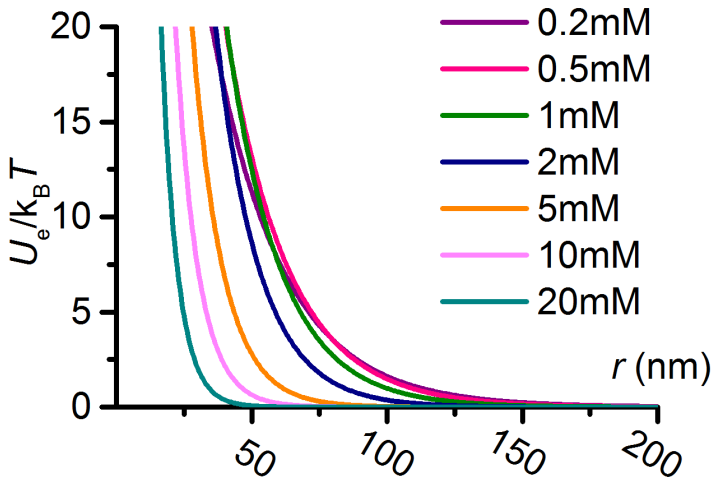

Supplementary Figure 10. Calculated U_e between two 100 nm AuNSs as a function of the inter-particle gap for variable CTAC concentrations.

2. Van der Waals interactions.

The Van der Waals interaction between two 100 nm AuNSs is given by

$$U_{vdw} = -\frac{Ar_p}{12r} \quad (6)$$

where A is the Hamaker constant. The retardation of the Hamaker constant of Au in water is taken into account, as shown in Supplementary Fig. 11a[11]. It was assumed that A becomes zero when the inter-particle distance is greater than 100 nm. The calculated van der Waals interaction potential is shown in Supplementary Fig. 11b.

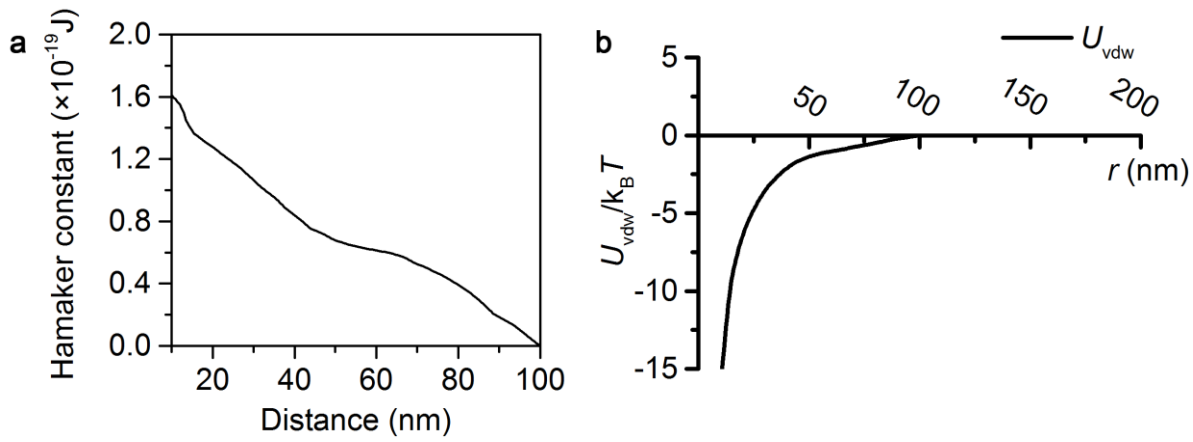

Supplementary Figure 11. Van der Waals interaction between two 100 nm AuNSs. a, Retarded Hamaker constant of Au in water as a function of the inter-particle gap. **b,** Calculated U_{vdw} between two 100 nm AuNSs as a function of the inter-particle gap.

3. Depletion attraction.

To interpret the depletion attraction potential between two 100 nm AuNSs trapped by OTENT in CTAC solution, we take into account several factors: (1) the CTAC molecules adsorb on the AuNS surface to modify its surface charge and the surface potential of the AuNSs is a function of the CTAC concentration; (2) CTAC micelles are treated as highly charged depletants and the electrostatic interaction between the micelles and the AuNSs is considered by introducing an effective micelle radius, which is also dependent on the CTAC concentration; (3) acting as depletants, micelles are much softer than the hard spheres. However, the optical heating of the laser on the thermoplasmonic substrate leads to the thermoosmosis (depletion) of the micelles and, therefore, complete micelle depletion is assumed here.

The depletion attraction is calculated with the depletion volume ΔV and the osmotic-pressure difference $\Delta \Pi$:

$$U_{\mathrm{d}} = -\Delta V \Delta \Pi \tag{7}$$

The depletion volume is given by[7,12]

$$\Delta V = \pi[(4/3)(r_p + r_d^{\,eff})^3(1-(3/4)(r_p + r_d^{\,eff} + r)(r_p + r_d^{\,eff})^{-1} + (1/16)(r_p + r_d^{\,eff} + r)^3(r_p + r_d^{\,eff})^{-3})] \quad (8)$$

where $r_d^{\,eff}$ is the effective micelle radius of the CTAC micelles, which is given by

$$r_d^{\,eff} = r_d + m\kappa^{-1} \quad (9)$$

where r_d is the hard-sphere radius of the micelles and *m* is an additional factor that arises from the micelle-particle interaction. To estimate $r_d^{\,eff}$, we calculated the electrostatic interaction between the CTAC micelles and the 100 nm AuNS by

$$U_e^{\,dp} = 4\pi\varepsilon\psi_d\psi_p \frac{r_d r_p}{(r_d + r_p + r_{dp})} \exp(-\kappa r_{dp}) \quad (10)$$

where ψ_d is the surface potential of the CTAC micelles, and r_{dp} is the surface-to-surface distance between the micelle and the AuNS. The interaction potential between a CTAC micelle and the 100 nm AuNS is shown in Supplementary Fig. 12. The effective micelle-particle distance is estimated at $U_e^{\,dp}$ = 1 k_BT, suggesting that *m* = 3.73 in the 10 mM CTAC solution.

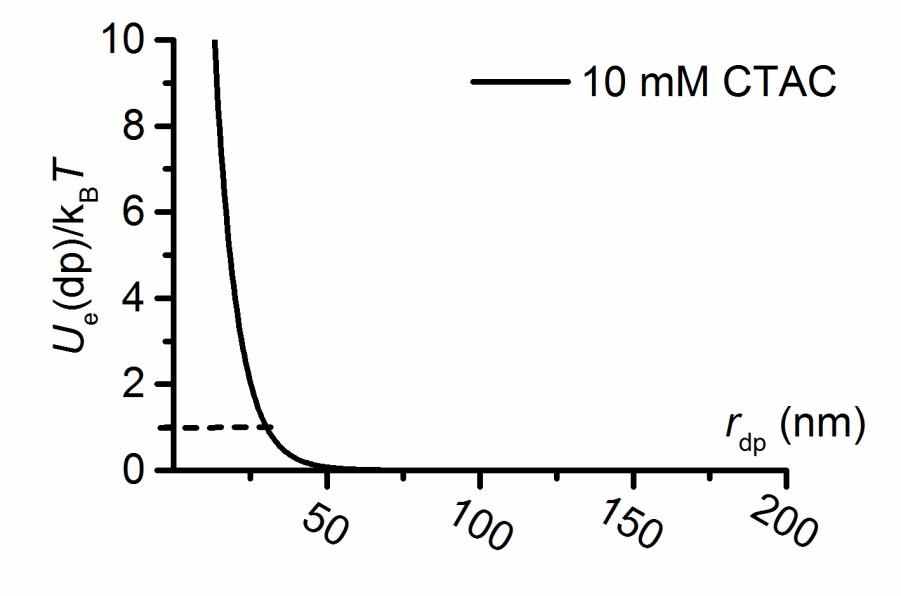

Supplementary Figure 12. Electrostatic interaction potential between the CTAC micelle and a single 100 nm AuNS as a function of the micelle-particle distance. The CTAC concentration is 10 mM. The dashed line shows $U_e^{dp} = 1\ k_BT$ and the r_{dp} value of the intersection point gives the effective micelle-particle gap.

We summarized the *m* value at different CTAC concentration in Supplementary Table 1, showing that the *m* value increases with CTAC concentration.

Supplementary Table 1. Calculated *m* value at different CTAC concentrations.

CTAC concentration (mM)	0.2	0.5	1	2	5	10	20
***m* value**	3.0	3.18	3.36	3.48	3.6	3.73	3.78

The osmotic-pressure difference $\Delta\Pi$ is a function of the micelle number density n:

$$\Delta\Pi = \beta n k_B T \tag{11}$$

where β is introduced as the depletion fraction because the micellar depletants are softer than the hard spheres. It should be noted that β is a function of the temperature gradient (or optical power of the heating laser). However, considering the optical power used in the experiment, we assume that complete depletion takes place and set $\beta = 100\%$. n is given by

$$n = \frac{N_A}{N_{agg}}(c_s - c_{cmc}) \tag{12}$$

where N_{agg} is the aggregation number of the CTAC micelles[13]. We summarized the depletion attraction potential U_d at different CTAC concentrations in Supplementary Fig. 13.

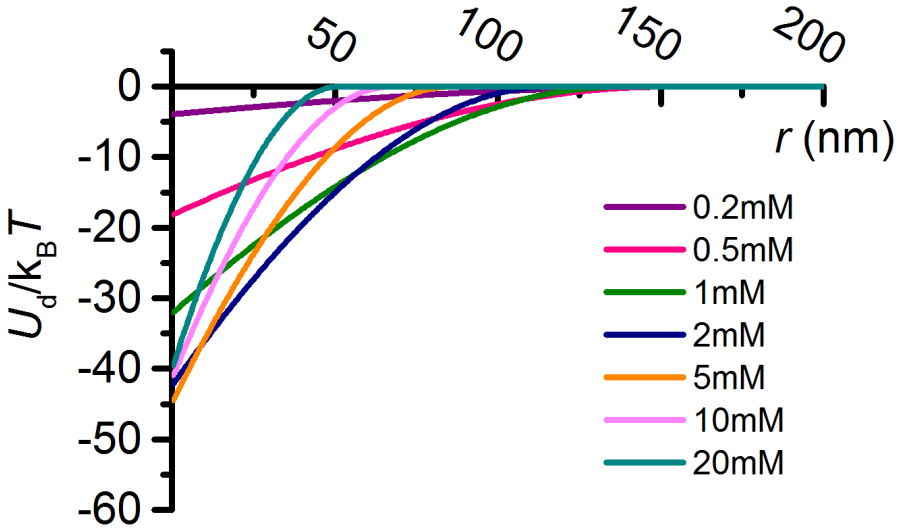

Supplementary Figure 13. Calculated U_d between two 100 nm AuNSs as a function of the inter-particle gap for variable CTAC concentrations.

Supplementary Note 4. Trapping of large nanoparticles *via* OTENT.

We also applied OTENT to trap larger metal nanoparticles, which exhibit strong light scattering and therefore experience a large optical scattering force. We succeeded in trapping 200 nm AuNSs and 400 nm AuNSs, the latter are the largest metal spheres we had at hand. Since the trapping force is proportional to the surface charge Q, we normalized the trapping stiffness of both 100 nm AuNSs and 200 nm AuNSs with regard to R^2, where R is the radius of the particles (Supplementary Figs. 14a and b). Interestingly, we can see that the normalized stiffness of 100 nm AuNSs is higher than that of 200 nm AuNSs, indicating that the trapping capability is improved for smaller particles. To explain the improved trapping capability for smaller particles, we simulated both in-plane and out-of-plane temperature gradients at heights of 50 nm and 100 nm above the thermoplasmonic substrate (Supplementary Figs. 14c and d), which are at the spherical centres for 100 nm AuNSs and 200 nm AuNSs, respectively. An increased temperature gradient is observed at the plane that is 50 nm above the substrate, providing an enhanced thermoelectric field according to equation 3. Therefore, in contrast to optical tweezers, which require a much higher optical power to trap smaller particles[14], OTENT is more efficient in trapping small nanoparticles at low optical power. We expect that OTENT could also trap metal microparticles. The upper size limit for metal particles exists for the distortion of temperature profiles by the trapped particles, which remains to be tested.

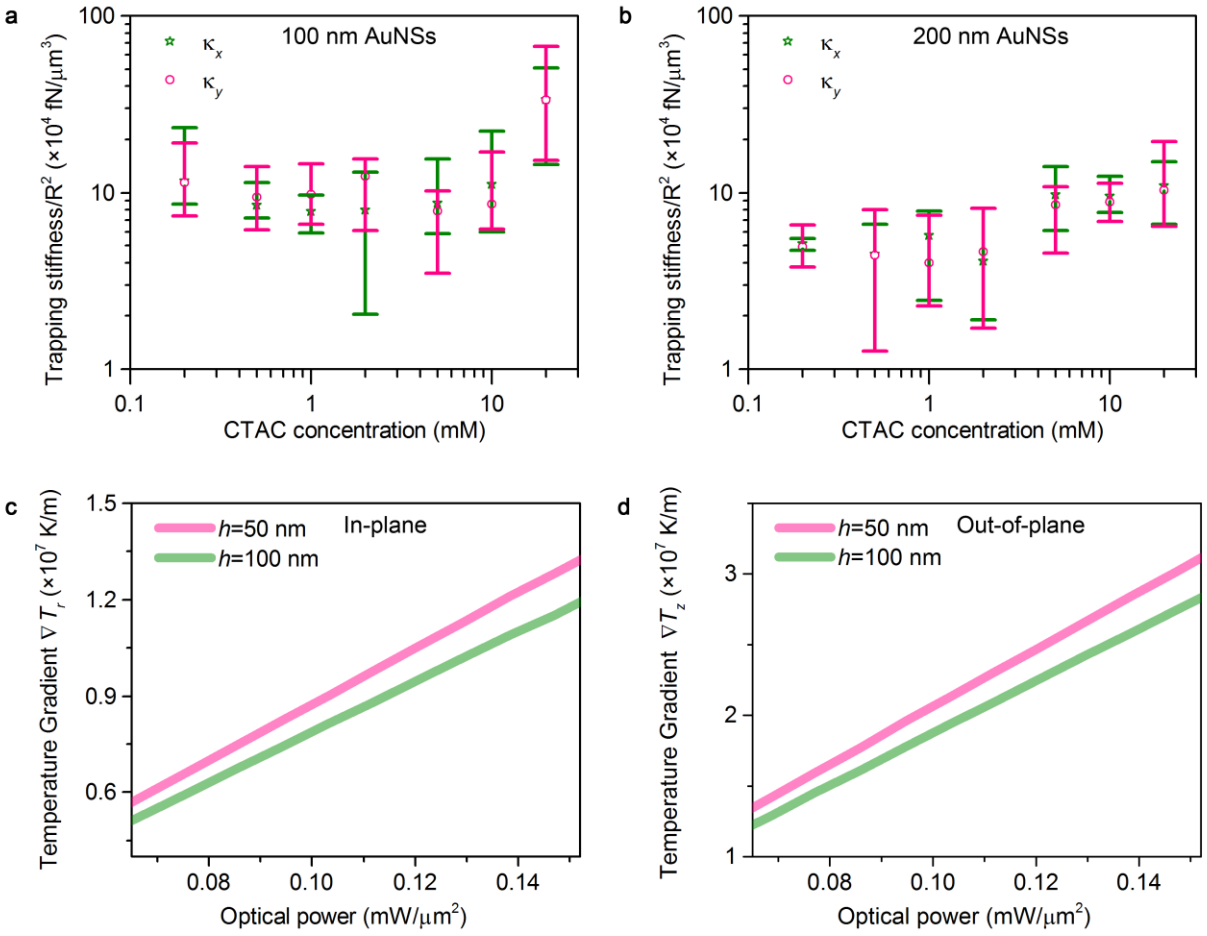

Supplementary Figure 14. Measured trapping stiffness of AuNSs and simulated temperature gradient at different heights. a, Trapping stiffness of 100 nm AuNSs normalized by R^2. **b**, Trapping stiffness of 200 nm AuNSs normalized by R^2. **c,** Simulated in-plane temperature gradients at heights of 50 nm and 100 nm above the substrate as a function of the incident optical power. **d,** Simulated out-of-plane temperature gradients at heights of 50 nm and 100 nm above the substrate as a function of the incident optical power. The heights of 50 nm and 100 nm correspond to spherical centres of trapped 100 nm AuNSs and 200 nm AuNSs.

Supplementary Note 5. Single-Nanowire Trapping and Rotation.

One-dimensional (1D) metal nanostructures with high aspect ratio (e.g. metal nanowires) can confine surface plasmons on the metal surfaces with longitudinal propagation, which are also known as surface plasmon resonators[15]. The multiple longitudinal plasmon resonances dramatically increase the absorption and scattering of light, which amplify the optical scattering force and make optical trapping extremely challenging[16-18]. With its low-power operation and versatile light management, OTENT can trap metal nanowires with precise location and orientation control. As shown in Supplementary Fig. 15a, we created a 1D optical image on the thermoplasmonic substrate to trap a single AgNW with 50 nm in diameter. Different from optical tweezers, which rely on highly focused laser beams, the generated thermoelectric field can be well controlled by rational design of the optical images projected onto the substrate. The thermoelectric field exerts a trapping force on the AgNW that tends to align it with the optical image. The alignment allows us to further control the nanowire orientation by rotating the optical image, as shown in Supplementary Fig. 15b (see Supplementary Movie 3 for the AgNW trapping and rotation). We further recorded the scattering optical images of the trapped AgNW excited with differently polarized light. When the polarization was tuned along the AgNW, the multiple longitudinal surface plasmons were excited (right panel in Supplementary Fig. 15c), with a bright scattering optical image observed. When the polarization was perpendicular to the AgNW, only the transverse mode (λ = 420 nm) can be excited, with the scattering intensity greatly suppressed (Supplementary Fig. 15d).

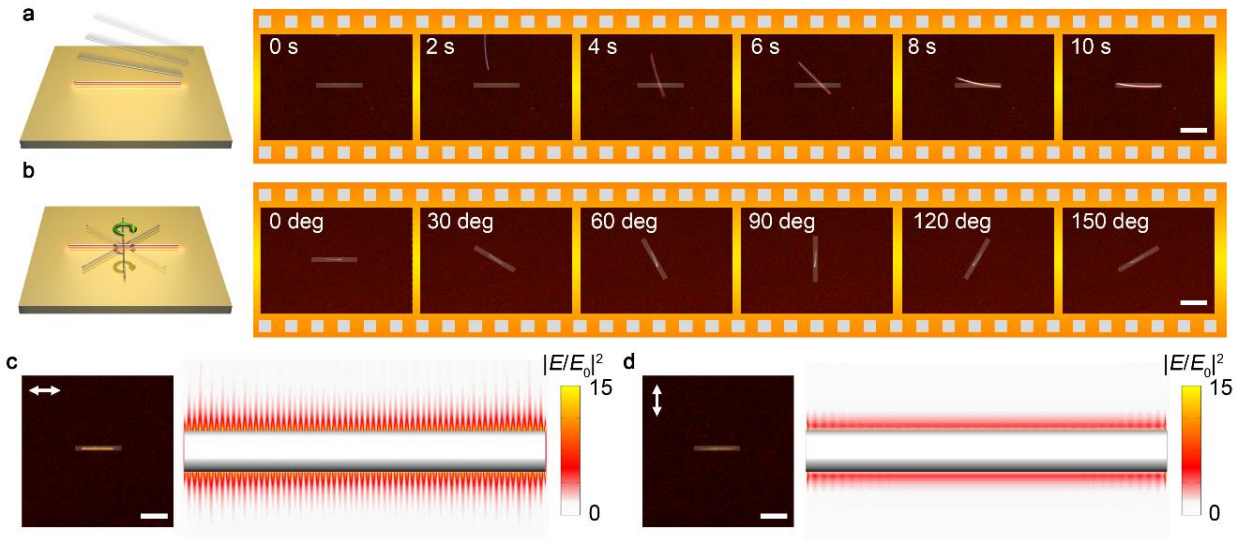

Supplementary Figure 15. Trapping and rotation of a single AgNW. a, Schematic illustration and successive optical images showing the trapping process of a single AgNW with a 1D optical image. **b,** Schematic illustration and successive optical images showing the rotation of a single AgNW with a 1D optical image. The grey line represents the 1D optical image. **c,** Dark-field optical image and simulated electric field intensity when longitudinal surface plasmons are excited along the nanowire (λ = 703 nm). **d,** Dark-field optical image and simulated electric field intensity when transverse surface plasmons are excited along the nanowire (λ = 420 nm). The AgNW in **c** and **d** has a length of 11.7 μm. The white arrows in the optical images of **c** and **d** show the polarization of the incident white light. Scale bars: 10 μm.

References

1. Eastman, E. D. Theory of the soret effect. *J. Am. Chem. Soc.* **50,** 283-291 (1928).

2. Würger, A. Thermal non-equilibrium transport in colloids. *Rep. Prog. Phys.* **73,** 126601 (2010).

3. Vigolo, D., Buzzaccaro, S. & Piazza, R. Thermophoresis and thermoelectricity in surfactant solutions. *Langmuir* **26,** 7792-7801 (2010).

4. Bregulla, A. P., Würger, A., Günther, K., Mertig, M. & Cichos, F. Thermo-osmotic flow in thin films. *Phys. Rev. Lett.* **116,** 188303 (2016).

5. Reichl, M., Herzog, M., Götz, A. & Braun, D. Why charged molecules move across a temperature gradient: The role of electric fields. *Phys. Rev. Lett.* **112,** 198101 (2014).

6. Lin, L., Peng, X., Wang, M., Scarabelli, L., Mao, Z., Liz-Marzán, L. M., *et al.* Light-directed reversible assembly of plasmonic nanoparticles using plasmon-enhanced thermophoresis. *ACS Nano* **10,** 9659-9668 (2016).

7. Iracki, T. D., Beltran-Villegas, D. J., Eichmann, S. L. & Bevan, M. A. Charged micelle depletion attraction and interfacial colloidal phase behavior. *Langmuir* **26,** 18710-18717 (2010).

8. Russel, W. B., Saville, D. A. & Schowalter, W. R. *Colloidal dispersions*. Cambridge University Press: Cambridge, 1989.

9. Pignolet, C., Euvrard, M., Foissy, A. & Filiâtre, C. Electrodeposition of latex particles in the presence of surfactant: Investigation of deposit morphology. *J. Colloid Interface Sci.* **349,** 41-48 (2010).

10. Tulpar, A., Subramanian, V. & Ducker, W. Decay lengths of double-layer forces in solutions of partly associated ions. *Langmuir* **17,** 8451-8454 (2001).

11. Biggs, S. & Mulvaney, P. Measurement of the forces between gold surfaces in water by atomic force microscopy. *The Journal of Chemical Physics* **100,** 8501-8505 (1994).

12. Edwards, T. D. & Bevan, M. A. Depletion-mediated potentials and phase behavior for micelles, macromolecules, nanoparticles, and hydrogel particles. *Langmuir* **28,** 13816-13823 (2012).

13. Roelants, E. & De Schryver, F. C. Parameters affecting aqueous micelles of ctac, ttac, and dtac probed by fluorescence quenching. *Langmuir* **3,** 209-214 (1987).

14. Hansen, P. M., Bhatia, V. K., Harrit, N. & Oddershede, L. Expanding the optical trapping range of gold nanoparticles. *Nano Lett.* **5,** 1937-1942 (2005).

15. Ditlbacher, H., Hohenau, A., Wagner, D., Kreibig, U., Rogers, M., Hofer, F., *et al.* Silver nanowires as surface plasmon resonators. *Phys. Rev. Lett.* **95,** 257403 (2005).

16. Yan, Z., Pelton, M., Vigderman, L., Zubarev, E. R. & Scherer, N. F. Why single-beam optical tweezers trap gold nanowires in three dimensions. *ACS Nano* **7,** 8794-8800 (2013).

17. Yan, Z., Sweet, J., Jureller, J. E., Guffey, M. J., Pelton, M. & Scherer, N. F. Controlling the position and orientation of single silver nanowires on a surface using structured optical fields. *ACS Nano* **6,** 8144-8155 (2012).

18. Tong, L., Miljković, V. D. & Käll, M. Alignment, rotation, and spinning of single plasmonic nanoparticles and nanowires using polarization dependent optical forces. *Nano Lett.* **10,** 268-273 (2010).